ARTICLE   OPEN

Indian Ocean warming as key driver of long-term positive trend of Arctic Oscillation

Yong-Cheol Jeong [1], Sang-Wook Yeh [1 ✉], Young-Kwon Lim[2,3], Agus Santoso [4,5,6] and Guojian Wang [4,7,8]

Arctic oscillation (AO), which is the most dominant atmospheric variability in the Northern Hemisphere (NH) during the boreal winter, significantly affects the weather and climate at mid-to-high latitudes in the NH. Although a climate community has focused on a negative trend of AO in recent decades, the significant positive trend of AO over the last 60 years has not yet been thoroughly discussed. By analyzing reanalysis and Atmospheric Model Inter-comparison Project (AMIP) datasets with pacemaker experiments, we found that sea surface temperature warming in the Indian Ocean is conducive to the positive trend of AO from the late 1950s. The momentum flux convergence by stationary waves due to the Indian Ocean warming plays an important role in the positive trend of AO, which is characterized by a poleward shift of zonal-mean zonal winds. In addition, the reduced upward propagating wave activity flux over the North Pacific due to Indian Ocean warming also plays a role to strengthen the polar vortex, subsequently, it contributes to the positive trend of AO. Our results imply that the respective warming trend of tropical ocean basins including Indian Ocean, which is either anthropogenic forcing or natural variability or their combined effect, should be considered to correctly project the future AO's trend.

npj Climate and Atmospheric Science (2022)5:56 ; https://doi.org/10.1038/s41612-022-00279-x

INTRODUCTION

Arctic oscillation (AO), also known as the Northern Hemisphere Annular Mode, is the most dominant atmospheric variability over the mid-to-high latitudes in the Northern Hemisphere (NH) during the boreal winter (December-January-February, hereafter, DJF)[1]. The spatial structure of AO is characterized by a seesaw-like pattern in the geopotential height (GPH) or sea level pressure (SLP) between the mid-latitude NH and the Arctic region, which indicates a redistribution of the air mass between these regions[1–3]. Concurrently, large-scale atmospheric circulation in the NH also varies due to the phase of AO and, consequently, it affects surface temperature as well as atmospheric circulation over several regions. For example, when AO is in a positive phase, zonal-mean zonal winds at mid-latitudes are shifted poleward and enhanced, resulting in warmer surface temperatures than normal over northern Eurasia, East Asia, and southeastern North America during boreal winter[2–8]. These characteristics are nearly reversed in AO negative phase as featured by cold winter over those regions in the strongest negative AO year, 2009/2010[9]. It is important to know how the AO phases vary in a changing climate because those regions are the most populated and industrialized regions at the mid-latitudes in the NH.

A previous study showed that an observed trend of AO since 1960 could not be statistically explained by atmospheric internal variability, which implies that external forcing exerted important influence on this trend[10]. As such, the climate community has sought to understand the physical processes affecting the AO's trend in a changing climate[11,12]. Some researchers have argued that an increase in greenhouse gases can force the AO toward its positive polarity by strengthening the meridional temperature gradient in the upper troposphere and lower stratosphere[13–15]. However, AO presented a negative trend from the late 1980s to the early 2010s[16,17]. Although such a negative trend of AO could be an atmospheric internal variability[18], it has been also suggested that an increase in vertical propagation of planetary waves, which is due to either Arctic sea ice loss along with Arctic amplification[19–23] or an increase in snow cover in the Eurasian continent[24–26], plays a role. While there has been a wealth of research on the AO's trend and its associated mechanisms[24,25,27–29], there have been fewer studies that have examined the mechanism explaining the AO's trend for a sufficiently long period of time.

We analyzed reanalysis datasets, Atmospheric Model Inter-comparison Project (AMIP) model datasets, and pacemaker experiments using an Atmospheric General Circulation Model (AGCM) to investigate a long-term trend of AO and associated physical mechanism. Unless stated otherwise in the text, the results were for the winter (DJF) season only. We defined winter as the three months from December to February for the SST data and atmospheric variables; therefore, 1958 winter indicates December 1958, January 1959, and February 1959.

RESULTS

A positive trend of Arctic oscillation

We first displayed the AO index for 1958–2017 from the observational sea level pressure data from the Met Office Hadley Centre (HadSLP2)[30] (Fig. 1a). Although a climate community has focused on a significant negative trend of AO from the late 1980s to the early 2010s[25] (green dashed line in Fig. 1a) and suggested that it is associated with the Arctic amplification[28], the most

[1]Department of Marine Science and Convergence Engineering, Hanyang University, ERICA, Ansan, South Korea. [2]NASA Goddard Space Flight Center Global Modeling and Assimilation Office, Greenbelt, MD, USA. [3]University of Maryland, Baltimore County, Baltimore, MD, USA. [4]Center for Southern Hemisphere Oceans Research (CSHOR), CSIRO Oceans and Atmosphere, Hobart, TAS, Australia. [5]Climate Change Research Center (CCRC), The University of New South Wales, Sydney, NSW, Australia. [6]Australian Research Council (ARC) Center of Excellence for Climate Extremes, The University of New South Wales, Sydney, NSW, Australia. [7]Frontier Science Center for Deep Ocean Multispheres and Earth System and Physical Oceanography Laboratory, Ocean University of China, Qingdao, China. [8]Qingdao National Laboratory for Marine Science and Technology (QNLM), Qingdao, China. ✉email: swyeh@hanyang.ac.kr
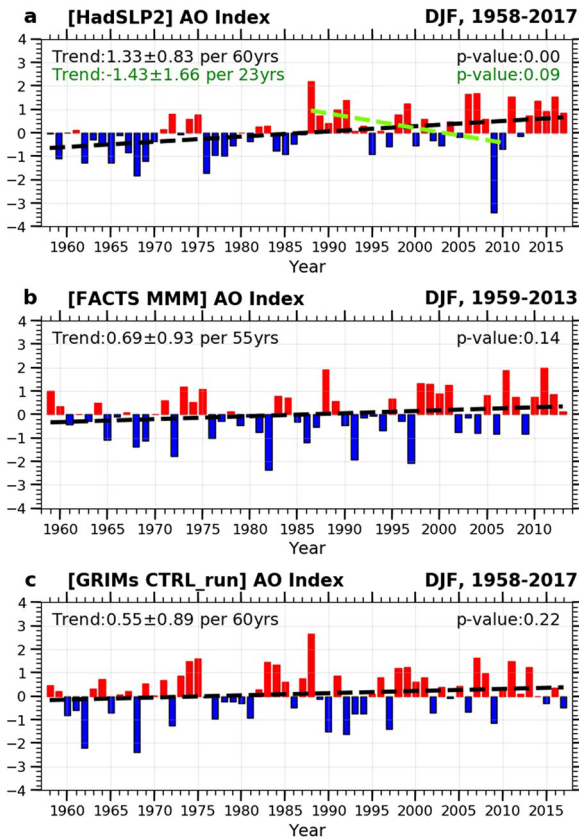
Fig. 1 Long-term trends of AO in observation and AMIP-type simulations. The AO index in (**a**) HadSLP2 data (1958–2017), (**b**) NOAA FACTS multi-model mean (Method, 1959–2013) and (**c**) GRIMs CTRL_run (Method, 1958–2017). The black dashed line indicates a linear trend of each AO index. The black numbers in the upper-left and upper-right sides of each panel denote the linear trend of AO index with a 95% confidence interval and its p-value, respectively. The green line and numbers in **a** denote the linear trend and the corresponding values during 1988–2010.

striking feature is that the observed AO index shows a statistically significant positive trend during the last 60 years (black dashed line in Fig. 1a). These positive trends are also found in other reanalysis datasets including the National Centers for Environmental Prediction and National Center for Atmospheric Research (NCEP/NCAR) reanalysis 1[31], and the Japanese 55-year (JRA-55) reanalysis data[32] (Supplementary Fig. 1a, b). It is noteworthy that the positive trend of AO is robust if the analyzed period is taken from the early 20th century (e.g., 0.89 per 88-year with a 95% confidence interval of ±0.71 and *p*-value of 0.02 in 1930–2017 period). While the climate community has been debating on whether or not global warming causes the negative trend of AO, the Arctic sea ice extent has gradually been decreasing (Supplementary Fig. 2a) with the continuous warming of the Arctic surface temperature since 1958 (Supplementary Fig. 2b). Therefore, the positive trend of AO during the last 60 years cannot be simply explained by sea ice loss along with Arctic amplification which may explain the negative trend of AO on decadal timescale.

On the other hand, researchers have shown that the observed AO variability in the last half of the 20th century could be forced by time-averaged tropical diabatic heating[33], which is usually reflected in either outgoing long-wave radiation (OLR) or precipitation[34] associated with the total sea surface temperature (SST). Figures 2a, b displays the SST trends in the tropics for 1958–2017 from the Met Office Hadley Centre SST data sets (HadISST data sets)[35] and NOAA Extended Reconstructed Sea

Surface Temperature version 5 (ERSSTv5)[36], respectively. The observed tropical SST has been warmed with the significant warming over the Indian Ocean and western Pacific in the 1958–2017 period[37–39]. In addition, the decreases in OLR, which is indicative of enhanced convective heating, are observed in the tropical Indian Ocean and the eastern tropical Pacific (Supplementary Fig. 3a, b). The correlations between AO index and OLR show that enhanced convective heating in some regions including the tropical Indian Ocean, the eastern tropical Pacific and the tropical Northern Atlantic is associated with the positive AO (Supplementary Fig. 3c, d). Note that the similar results are obtained after removing the trend although there are some discrepancies in detailed structures (Supplementary Fig. 3e, f). Therefore, it is necessary to further analyze whether tropical SST forcing with enhanced convection in a long-term period is conducive to the positive trend of AO.

To examine this notion, we analyzed AMIP-type simulations, which is useful for exploring atmospheric responses to underlying SST forcing. The AMIP-type simulations derived by three different climate models are obtained from the National Oceanic and Atmospheric Administration (NOAA) Facility for Weather and Climate Assessments (FACTS; Method)[40]. Each model is forced with the same historical forcing including SST, sea ice concentration (SIC) and greenhouse gas concentration with its own number of ensemble members (Supplementary Table 1), and we analyzed the multi-model mean (MMM) atmospheric variables and ensemble mean atmospheric variables simulated in each AGCM to examine the role of SST forcing with exclusion of the role of internal variability in the climate system (Method). The MMM AO index from NOAA FACTS displays a positive trend although it is only marginally statistically significant (Fig. 1b). All three AMIP-type simulations from NOAA FACTS also display a positive AO trend in their respective ensemble means (Supplementary Fig. 1c–e) although their statistical significances are not significant except for the GEOS-5 model at a 90% confidence level.

We also conducted AMIP-type simulations using the Global/Regional Integrated Model system (GRIMs)[41] in which historical SST is prescribed in the globe with 10 ensemble members (hereafter, referred to as CTRL_run and see also Supplementary Table 2) (Method). Here, we prescribed the monthly climatological SIC with a seasonal cycle and fixed the CO_2 concentration (348 ppm) to remove the effects of changes in the SIC and CO_2 concentration (Method), which is different from NOAA FACTS AMIP-type simulations. Similar to the NOAA FACTS AMIP-type simulations, the positive trend of AO is simulated in GRIMs CTRL_run, although it is not statistically significant (Fig. 1c). Despite a lack of strong statistical significance, there is a tendency of positive trends across the AMIP-type simulations, and we infer that the tropical SST forcing contributes to the positive trend of AO.

The precipitations in NOAA FACTS MMM and GRIMs CTRL_run significantly increase over the tropical Indian Ocean and the western Pacific Ocean (Fig. 2c, d), which is consistent to some extent with the OLR trend in the reanalysis datasets (Supplementary Fig. 3a, b). The reason of why we analyzed the precipitation data instead of OLR is because the OLR data is not available in the NOAA FACTS AMIP-type simulations. It is also found that there are various regions including the tropical Indian Ocean, the subtropical Pacific and the tropical Northern Atlantic Ocean where the positive correlations between AO index and precipitation are significant in both FACTS MMM and GRIMs CTRL_run (Fig. 2e, f). Similar results are obtained in each individual NOAA FACTS AMIP-type simulation (Supplementary Fig. 4). Considering both significant increase in tropical convection activities and significant positive correlation between convection activities and AO in reanalysis and AMIP-type simulations (Fig. 2, Supplementary Figs. 3, 4), we infer that the increases in SST-forced convection activities over the tropical Indian Ocean can drive the positive trend of AO.
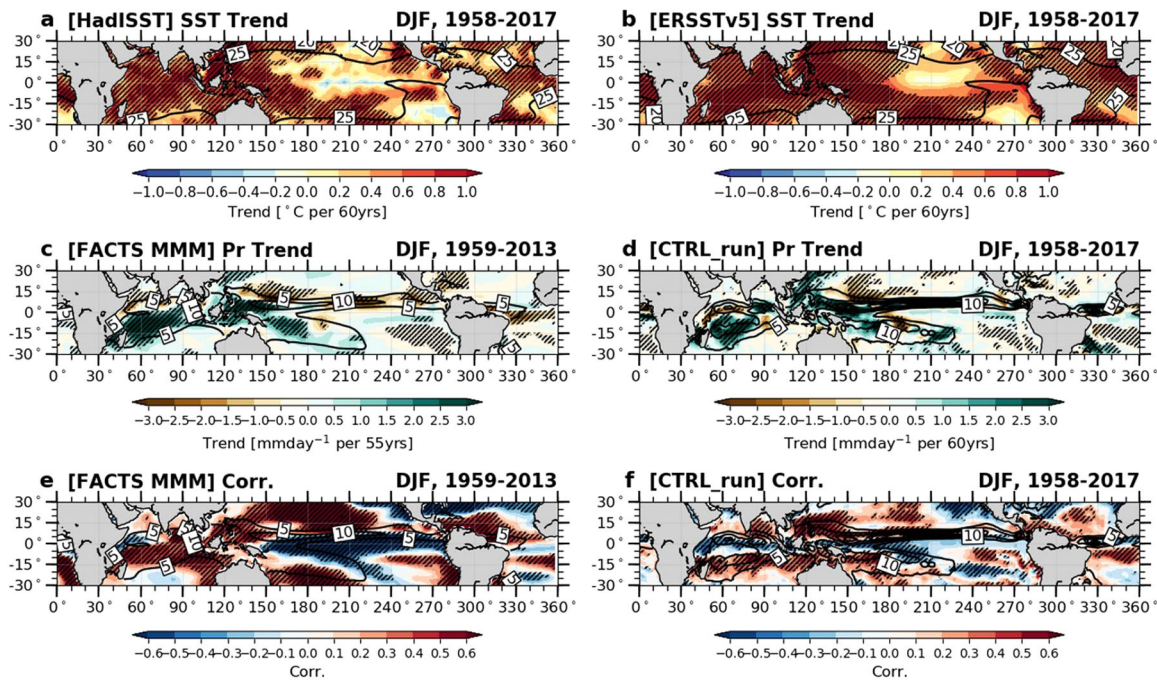
Fig. 2 Long-term trends of observed SST and simulated precipitation with its relationship with AO. The linear trend (shading) of the observed SST (1958–2017) in DJF from (**a**) HadISST and (**b**) ERSSTv5 with climatological SST (contour, unit: °C) in each dataset. The linear trend (shading) of simulated precipitation in DJF in (**c**) NOAA FACTS multi-model mean (1959–2013) and (**d**) GRIMs CTRL_run (1958–2017) with climatological precipitation (contour, unit: mmday^{-1}) in each dataset. The correlation coefficients between simulated AO and precipitation in (**e**) NOAA FACTS multi-model mean and (**f**) GRIMs CTRL_run with climatological precipitation (contour, unit: mmday^{-1}) in each dataset. In all figures, black hatched regions indicate a statistically significant region at a 95% confidence level.

On the other hand, the significant positive correlations over the subtropical Pacific and the tropical Northern Atlantic Ocean do not accompany with the long-term increase in precipitation (Fig. 2c–f, Supplementary Fig. 4). However, the correlation analysis does not imply causality, and the impact of SST forcings outside the IO cannot be thoroughly excluded based on the correlation analysis only. To overcome this, we further conducted additional pacemaker experiments in which SSTs are prescribed in specific tropical regions using GRIMs (Method).

Pacemaker experiments

The pacemaker experiments consist of four experiments with 10 ensemble members in which the historical SST is prescribed in the tropical Indian Ocean (IO_run), tropical Western Pacific (WP_run), tropical Eastern Pacific (EP_run) and tropical Atlantic Ocean (AT_run) (Supplementary Table 2). The details of geographical regions in which historical SST is prescribed in each experiment are shown in Supplementary Fig. 5. Except for the SST, other forcings such as SIC and CO_2 concentration in all pacemaker experiments are identical to the GRIMs CTRL_run. All results presented here are derived using the ensemble mean atmospheric variables.

The AO index simulated in each experiment is shown in Fig. 3. The only IO_run presents a significant positive trend of AO (Fig. 3a and Table 1), which is consistent to some extent with the role of the Indian Ocean warming in the positive trend of North Atlantic Oscillation (NAO) in the last half of the 20th century[42–44]. In contrast, the WP_run and AT_run simulate a statistically significant negative trend of AO index (Fig. 3b, d), and there is no significant trend in AO index in the EP_run (Fig. 3c). The opposite AO trend between the IO_run and WP/AT_runs might explain the relatively weak positive trend of AO in the CTRL_run (Fig. 1c). Indeed, the additive combination of AO's linear trends in four experiments (IO, WP, EP, and AT_run) is 0.08 per 60-year (Table 1). This implies that the significant contribution of IO on the positive AO trend is cancelled by that of other oceans, resulting in an insignificant AO trend in CTRL_run (Fig. 1c). However, 0.08 per 60-year is much smaller than the linear trend of AO in CTRL_run, 0.55 per 60-year (Table 1), which might be due to the notion that the AO variability simulated in CTRL_run could be explained by both linear and non-linear processes from individual oceans. Such cancellation effect from individual oceans also potentially occurs in the AMIP-type simulations from NOAA FACTS which also exhibit a less significant positive trend of AO index (Fig. 1b and Supplementary Fig. 1c–e). By the same token, the significant linear trend of AO in the reanalysis data sets (Fig. 1a and Supplementary Fig. 1a, b) might imply that the influence of the Indian Ocean SST forcing is dominant in the real system.

To explore the atmospheric structures in response to individual ocean SST forcing, we display the linear trend of 500hPa geopotential height (Z500) in each experiment (Fig. 4). Supplementary Fig. 6 further displays the linear trend of 200hPa geopotential height (Z200) and SLP in each experiment. The spatial pattern of Z500 trend in IO_run (Fig. 4a) is similar to a typical structure of positive AO. This contrasts with those in WP_run (Fig. 4b) where the negative AO's structure is dominant. On the other hand, the spatial patterns of Z500 in EP run and AT run are far from that of either positive or negative AO (Fig. 4c, d). It is noteworthy that the atmospheric responses in IO/WP_runs are stronger than those in EP/AT_runs (Fig. 4 and Supplementary Fig. 6). It might be because the amplitude of the SST trend is the greatest (Supplementary Fig. 5) and the climatological SST magnitude is also greater in the IO and WP regions than that in other two regions. In addition, because the IO is right below the South Asia subtropical jet, the strongest tropospheric jet in the NH, it may have a larger impact by how it impacts this jet and the associated NH atmospheric circulation. Indeed, the spatial structure of stationary wave anomalies from the northern Indian continent to Arctic region is distinct in IO run (Fig. 4a), which can be also seen from the regressed Z500 onto the precipitation
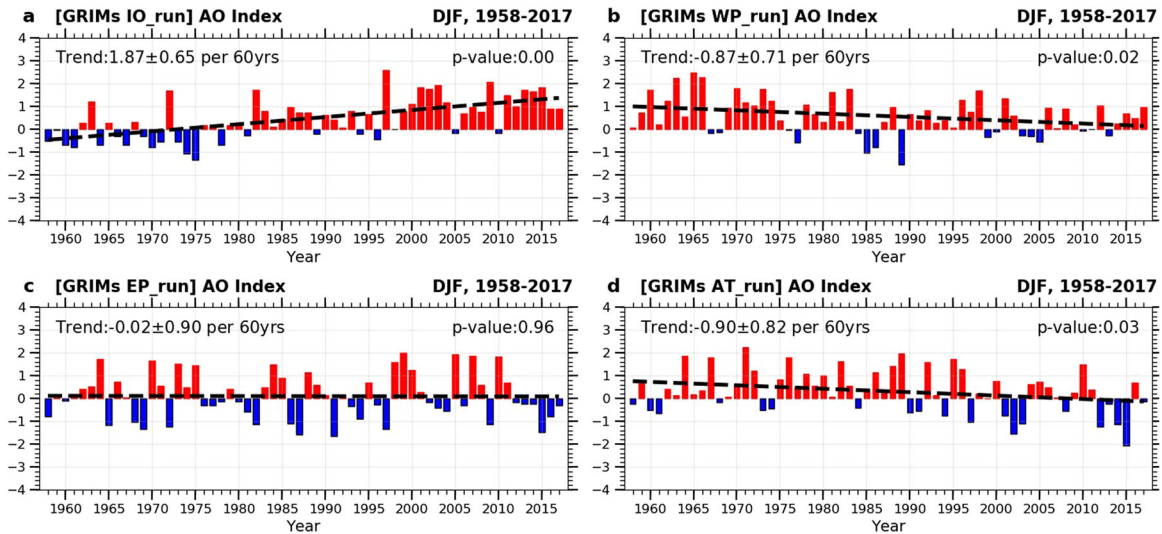
Fig. 3 Long-term trends of AO in each pacemaker experiment using GRIMs. The AO indices in (**a**) IO, (**b**) WP, (**c**) EP, and (**d**) AT runs in the period of 1958–2017. The black dashed line indicates a linear trend of each AO index. The number in lower-right sides of each panel denotes a *p*-value of the linear trend. The values of the linear trends and their 95% confidence intervals are summarized in Table 1.

Table 1. The linear trends of idealized GRIMs experiments.

Exp.	CTRL	IO	WP	EP	AT	IO + WP + EP + AT
Linear trend (60 years^{-1})	0.55 (±0.89)	1.87 (±0.65)	−0.87 (±0.71)	−0.02 (±0.90)	−0.90 (±0.82)	0.08

The linear trend of AO in each idealized GRIMs experiment. The number in parenthesis indicates a 95% confidence interval of the linear trend in each experiment.

variability averaged in Indian Ocean without the linear trend in IO run (Supplementary Fig. 7a). Note that the pattern correlation between them is 0.88, which is significantly high. This result implies that the increased precipitation over Indian Ocean caused a trend of Z500 with a positive AO's structure by generating stationary wave anomalies from the Indian continent into Arctic.

Physical processes of the Indian SST warming on a positive AO trend

To examine how the SST forcing with enhanced convective forcing over the Indian Ocean leads to the positive trend of AO, we introduced an IO index, which is defined as the precipitation anomaly averaged in the western-to-central southern Indian Ocean (50°E–90°E, 15°S–5°S; yellow box in Fig. 5a, b) where a significant increase in precipitation occurs due to the Indian Ocean warming (Fig. 5a, b). We selected 15°S–5°S to define the IO index even though the precipitation significantly increases over 30°S–5°S in the IO_run (Fig. 5a). This is because a significant decreasing trend of OLR is dominant between 15°S and the equator in the reanalysis datasets (Supplementary Fig. 3a, b). It should be noted that the overall results are consistent if the IO index is defined over 30°S–5°S.

The regressed pattern of precipitation onto the IO index is characterized by a meridional tripolar structure (Supplementary Fig. 7b), which implies that the IO index explains the linear trend of precipitation over the entire Indian Ocean (Fig. 5a). This meridional tripolar structure can be explained by atmospheric vertical motions associated with the IO index (Supplementary Fig. 7c). Due to the enhanced convection over the western-to-central southern Indian Ocean, convection activities are suppressed at the equator and enhanced north of the equator (Supplementary Fig. 7c), which results in a decrease and increase in precipitation along the equator and north of the equator, respectively (Fig. 5a and

Supplementary Fig. 7b). Thus, the meridional tripolar structure of precipitation over the Indian Ocean is largely explained by the increase in precipitation in the western-to-central southern Indian Ocean.

The standardized IO index and AO index in DJF in the IO_run are shown in Fig. 5c. The correlation coefficient between the two indices is 0.78 with the linear trend and 0.66 without the linear trend, which are all statistically significant at the 99% confidence level. This may indicate that increase in precipitation in the western-to-central southern Indian Ocean plays an important role in the positive trend of AO. Note that when the same calculation is applied to the results from NOAA FACTS AMIP-type simulations, the correlation coefficients are between 0.33 and 0.64 with the linear trend and between 0.30 and 0.63 without the linear trend, which are all statistically significant at least at the 95% confidence level (Supplementary Table 3).

The changes in atmospheric circulation associated with AO can be seen in the zonal-mean structure, because AO has a nearly zonally-symmetric structure[1,4]. Figure 5d displays the linear trend of zonal-mean zonal wind in the IO_run. The zonal-mean zonal wind has been shifted poleward due to the tropical Indian Ocean SST forcing, which corresponds to the positive trend of AO[2,45–48]. The poleward shift of zonal winds is also seen in the spatial structure of zonal wind trend at 200hPa (U200) in IO_run where it is dominant in Eurasian continent, the western Pacific and the northern Atlantic Ocean (Supplementary Fig. 8a). By applying the budget diagnostics of the zonal-mean zonal wind[49] (Methods), we found that the forcing by momentum flux convergence by the stationary waves plays a significant role in the poleward shift of zonal-mean zonal wind in the IO_run (Fig. 5e), and its role primarily arises from the horizontal term (Methods and Supplementary Fig. 9a, b). A poleward shift of zonal-mean zonal wind is dynamically consistent with the spatial pattern of the linear trend
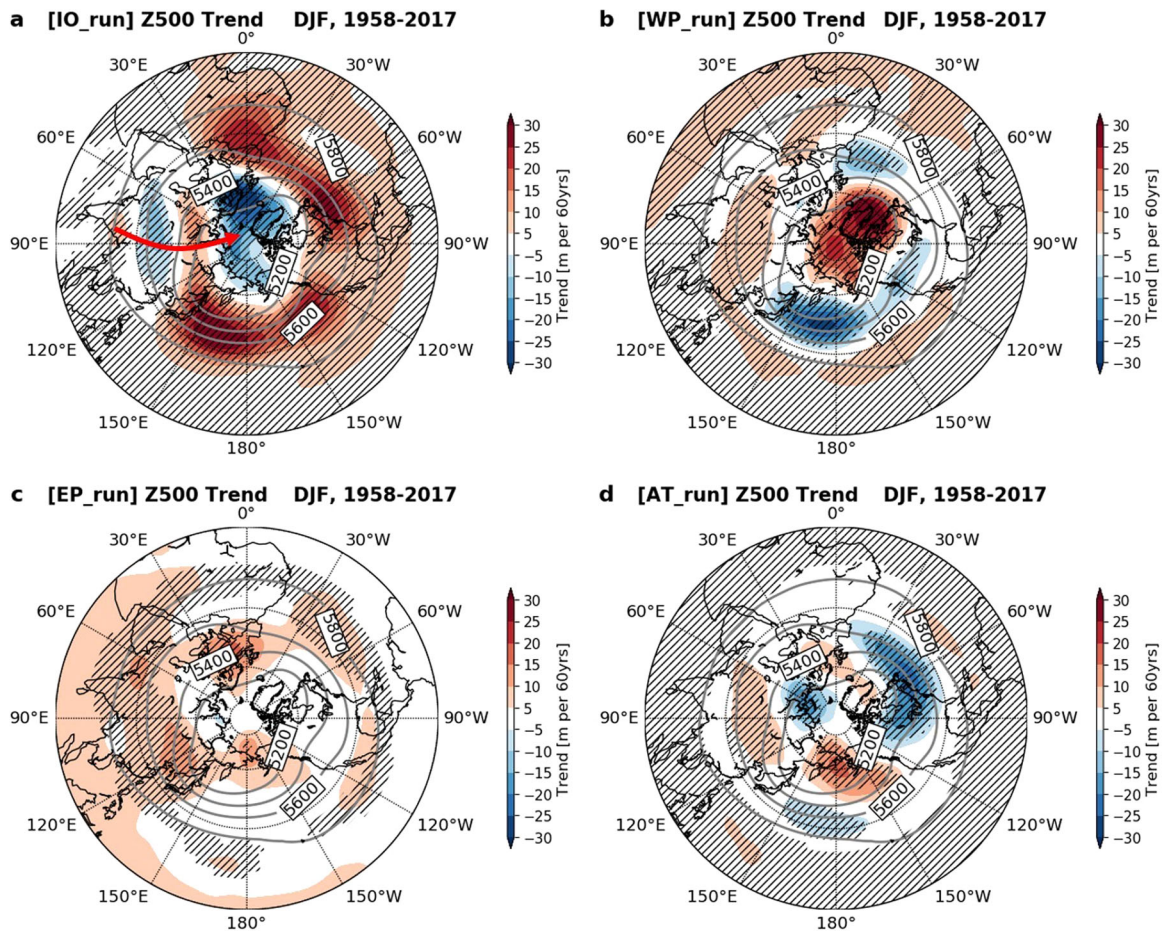
Fig. 4 Long-term trends of 500hPa geopotential height in each pacemaker experiment using GRIMs. The linear trends of 500hPa geopotential height (Z500) (shading) in (**a**) IO, (**b**) WP, (**c**) EP, and (**d**) AT runs with the climatological (1958–2017) Z500 (contour, unit: meter). The black hatched regions indicate statistically significant regions at a 95% confidence level. The red arrow in Fig. 4a indicates stationary wave anomalies from the northern Indian continent to Arctic region.

of Z500 and Z200 (Fig. 4a and Supplementary Fig. 6a) which favors to induce momentum flux convergence north of 45°N (Fig. 5e). A similar result is also obtained from the regressed maps including Z500, zonal-mean zonal winds and Z200 onto the IO index in the IO_run (Supplementary Figs. 7a, 9c–e, and 10a). This implies that the increase in convective forcing due to the Indian Ocean warming is an important dynamic driver for the positive trend of AO. On the other hand, the forcing by the momentum flux convergence by the transient eddies plays a smaller role (Supplementary Fig. 9f). In addition, the Coriolis torque is considered to be a response to stationary and transient terms, and the advection of the zonal-mean wind by mean meridional circulation is quite small compared to the stationary and transient terms[47,49] (Supplementary Fig. 9g, h).

The poleward shift of zonal-mean zonal winds in IO_run, however, is widespread latitudinally and vertically compared to the linear trend of momentum flux convergence by the stationary waves in IO_run (Fig. 5d, e), which may imply that the other process contributes to the poleward shift of zonal-mean zonal winds and the positive trend of AO in IO_run. In addition to the role of stationary waves in the troposphere, we also emphasized the role of troposphere-stratosphere coupled processes, which is associated with the IO warming, in the positive trend of AO. In IO_run, there is the significant positive trend of Z500 over the North Pacific (Fig. 4a) where the climatological low pressure with a zonal wave number 1 is located[21,50]. Thus, the positive trend of Z500 over the North Pacific is out-of-phase with the climatological

zonal wavenumber 1 structure, which can reduce an upward propagating wave activity flux at 100hPa (WAF$_z$100) through destructive interference[51]. Indeed, the climatological upward WAF$_z$100 from the eastern Siberia to the North Pacific[51,52] is reduced in IO_run (Fig. 6a). It should be noted that the significant negative trend of WAF$_z$100 is also noticeable over northeastern Europe where climatological weak upward WAF$_z$100 is located (Fig. 6a). Reduced upward WAF$_z$100 disrupts a stratospheric polar vortex to a less extent, which can play a role in strengthening of the stratospheric polar vortex (Fig. 6b). This subsequently contributes to the poleward shift of the zonal-mean zonal wind with a positive trend of AO in IO_run by a downward propagation[45]. It is noteworthy that the spatial structures of the regressed WAF$_z$100 and Z100 onto the IO index are consistent with those of linear trends of the corresponding variables, respectively (Fig. 6 and see also Supplementary Fig. 10b, c). This indicates that the increase in convective forcing due to the Indian Ocean warming plays a role to drive a positive trend of AO via troposphere-stratosphere coupled processes.

DISCUSSION

In recent decades, AO has displayed a significant negative trend. The climate forcing related to the Arctic amplification affected this negative trend of AO[19,20,25,28]. However, AO has displayed a significant positive trend in the long-term period (1958–2017), which cannot be explained by the Arctic amplification along with
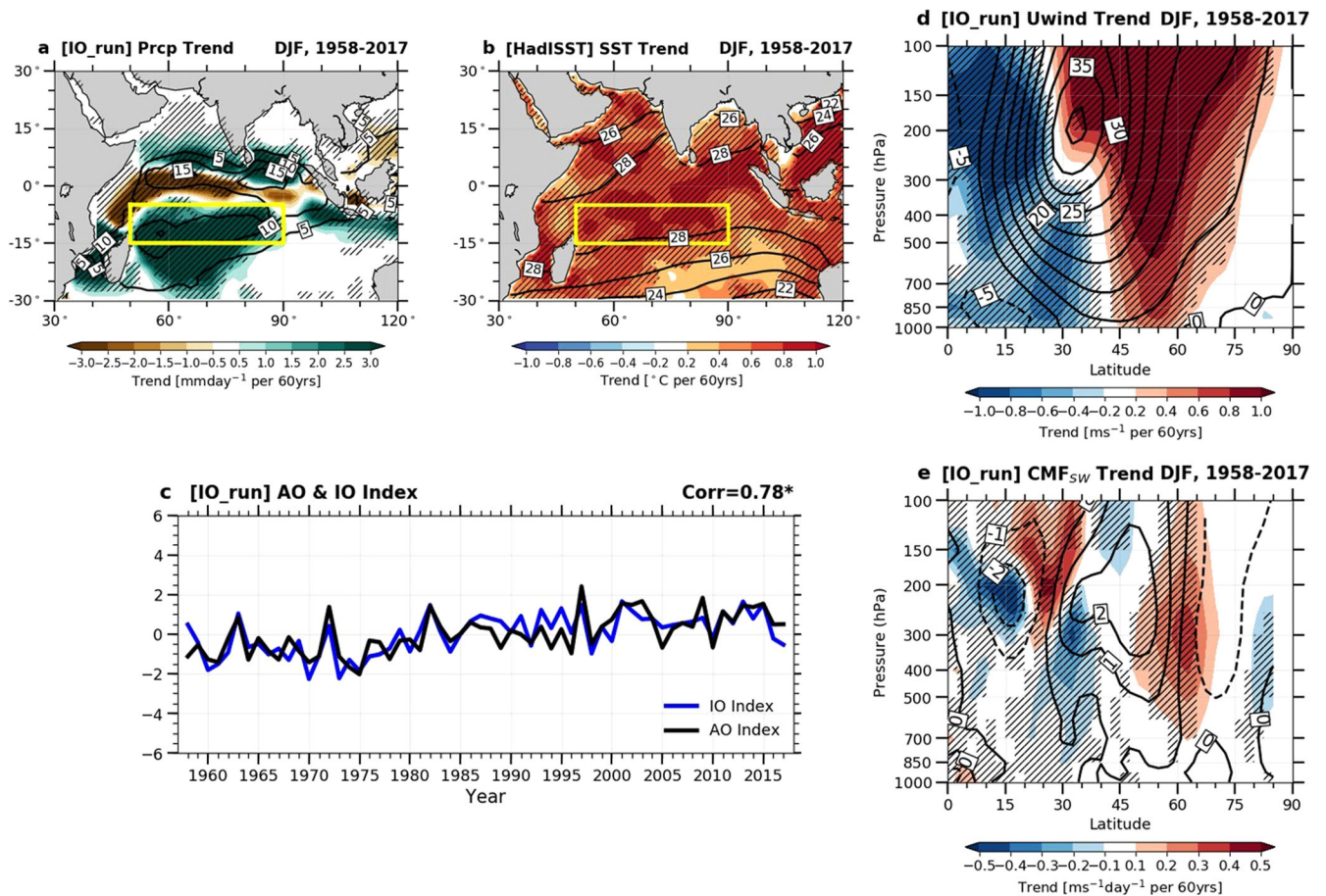
Fig. 5 Long-term trends of precipitation and zonal-mean zonal winds in the IO_run. a The linear trend of precipitation in DJF in IO_run (shading) with the climatological precipitation (contour, unit: mmday^{-1}) and **b** the linear trend of the observed SST in DJF in HadISST data (shading) with the climatological SST (contour, unit: °C). **c** Time-series of AO index and area-averaged precipitation anomalies in the western-to-central Indian Ocean (IO index, yellow box in Fig. 5a, b). Both indices are standardized and the correlation coefficient (Corr) between two indices is statistically significant at a 99% confidence level (*). **d** The linear trend of zonal-mean (0°–360°E) zonal winds in DJF in IO_run (shading) with the climatological zonal-mean zonal winds (contour, unit: ms^{-1}) and **e** the linear trend of convergence of momentum flux by the stationary waves (CMF$_{SW}$) in DJF in the IO_run (shading) with the climatological CMF$_{SW}$ (contour, unit: ms^{-1}day^{-1}). In all figures, the black hatched regions indicate statistically significant regions at a 95% confidence level.

sea ice loss. In the present study, we showed that the tropical Indian Ocean SST forcing plays a role in the positive trend of AO by modulating the convergence of momentum flux due to stationary waves in the troposphere and the troposphere-stratosphere coupled processes including the strengthening of stratospheric polar vortex. This was demonstrated by conducting AMIP-type experiments using GRIMs forced with the observed SSTs over different tropical regions, obtaining positive AO trend only when the forcing is in the tropical Indian Ocean (Fig. 3). In this study, we did not consider the effect of sea ice loss as well as Arctic amplification in the sufficiently long-term period (Supplementary Fig. 2), in addition, the main results were obtained from the analysis of AMIP experiments using a single AGCM. In spite of this caveat, we argue that the tropical Indian Ocean SST forcing plays an important role in the long-term positive trend of AO although climate forcings associated with the sea ice loss and Arctic amplification could be influential to that in the sub-period.

It was also found that the magnitude of positive trend of AO was more significant in reanalysis data sets than AMIP-type simulations (Fig. 1 and Supplementary Fig. 1). We do not exclude the notion that the counteracting influence of SST warming in other basins was not very active relative to IO warming in the observation, simply due to internal variability. And as a

consequence the influence of IO warming would be less in AMIP-type simulation compared to the observation. On the other hand, a previous study showed that local extratropical air-sea interactions over North Atlantic region can amplify an AO response to tropical Pacific SST forcing[53]. A lack of these air-sea interactions might also cause the less significant positive trend of AO in AMIP-type simulations.

The mid-to-high latitude climate is largely affected by AO phase in boreal winter. In boreal winter with a positive AO, the poleward shift of zonal winds can result in a warm and calm winter in the industrialized and populated regions, such as East Asia and southeastern North America[1,4]. Such climate condition can favor a severe haze event and air pollution by weakening horizontal and vertical ventilations particularly in East Asia[54–57]. In addition, a recent study showed that the anomalous warm temperature associated with a positive AO during winter can promote wildfires in early spring over eastern Siberia[5]. Thus, a long-term positive trend of AO can exert various socio-economic impacts. It has been suggested that Indian Ocean warming during the present-day period can be attributed to various reasons, such as direct greenhouse gas forcing and changes in atmospheric and ocean circulations induced by greenhouse gas forcing[58–61]. Given that the Indian Ocean is sensitive to external forcing due to shallow
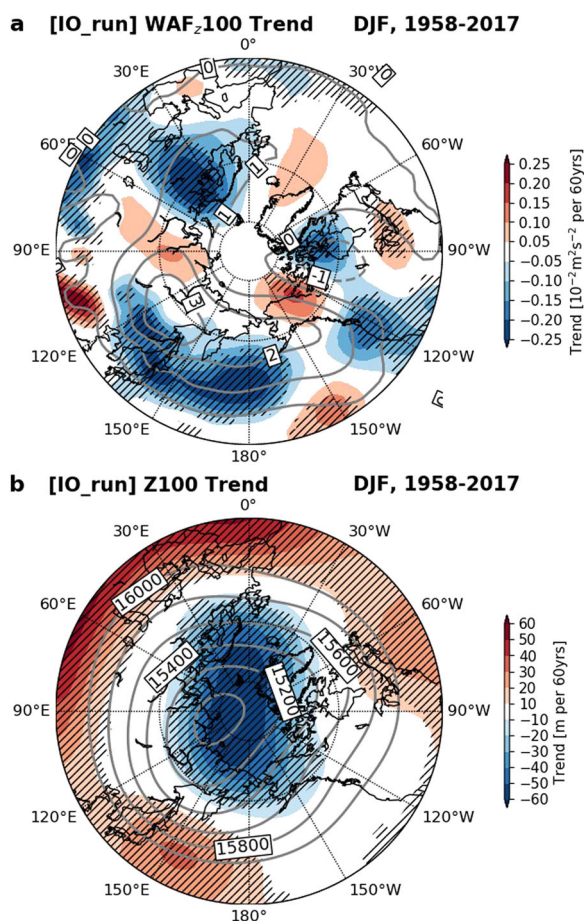
Fig. 6 Long-term trends of vertical wave activity flux and polar vortex in the IO_run. a The linear trend of vertical wave activity flux at 100hPa (WAF$_z$100) (shading) with the climatological (1958–2017) WAF$_z$100 (contour, unit: 10^{-2}m^{2}s^{-2}) and (**b**) the linear trend of geopotential height at 100hPa (Z100) (shading) with the climatological Z100 (contour, unit: meter) in IO_run. The positive WAF$_z$ in Fig. 6a indicates the upward WAF$_z$. The black hatched regions in Fig. 6a, b indicate statistically significant regions at a 95% confidence level.

mixed layer depth[62] and relatively weaker SST variability compared to other ocean basins[63], it is expected that the tropical Indian Ocean SST will keep increasing in the future climate[61,64]. Therefore, AO is expected to have a positive trend in the future climate. However, the SST warming in other tropical basins is also expected in the future climate[64–66] and the total trend of future AO will depend on the amplitude of the tropical SST warming in the respective ocean basin. Therefore, it is necessary to carefully examine how the SST in each tropical ocean basin will respond to anthropogenic forcing in order to explain the linear trend of AO in the future climate.

METHODS

Reanalysis datasets and AMIP datasets

In this study, we used two reanalysis datasets including the National Centers for Environmental Prediction and National Center for Atmospheric Research (NCEP/NCAR) reanalysis 1 dataset[31] and the Japanese 55-year (JRA-55) reanalysis dataset[32] for 1958–2017. The observational sea level pressure (SLP) data from the Met Office Hadley Centre (HadSLP2)[30] was also used to investigate a linear trend of AO during the same period. In addition, we used monthly sea surface temperature (SST) and sea ice concentration (SIC) datasets from the Met Office Hadley Centre (HadISST data sets)[35] to investigate an linear trend of the SST and SIC in the same period. The monthly SST data sets from the NOAA Extended Reconstructed

Sea Surface Temperature version 5 (ERSSTv5)[36] were also used to investigate the linear trend of SST.

In addition to the reanalysis and observation datasets, we also used the Atmospheric Model Inter-comparison Project (AMIP) simulated dataset, which was provided by the National Oceanic and Atmospheric Administration (NOAA) Earth System Research Laboratory (ESRL) Facility for Climate AssessmenTS (FACTS) (https://psl.noaa.gov/repository/facts)[40]. The various atmospheric models were forced by the observed historical SST and SIC[67]. The greenhouse gas concentrations were also time varying, which were the same values as the Coupled Model Intercomparison Project phase 5 (CMIP5) recommendations[68]. Among these, we selected three available models including GEOS-5[69], GFDL-AM3[70], and LBNL-CAM5.1[71] that simulate a long-term period comparable to reanalysis and observational data (Supplementary Table 1). The GEOS-5 simulates a historical 144-year (1871–2014) period with $1.25° \times 1.25°$ horizontal resolution and 72 vertical layers. The GFDL-AM3 simulates a historical 145-year (1870–2014) period with about $1.9° \times 1.9°$ horizontal resolution and 48 vertical layers. The LBNL-CAM5.1 simulates a historical 55-year (1959–2014) period with about $1.0° \times 1.0°$ horizontal resolution and 25 vertical layers. The GEOS-5 and GFDL-AM3 have 12 ensemble members, and LBNL-CAM5.1 has 50 ensemble members. Although the simulated period is diverse across the model, the analysis was conducted in the same historical 55-year (1959–2013) period in all models, which is a comparable period to that in the reanalysis datasets. All results from AMIP simulations are derived from ensemble mean atmospheric variables, and the results from multi-model mean (MMM) atmospheric variables are also presented in this study. The MMM atmospheric variables are obtained as the average of the corresponding ensemble mean atmospheric variables of LBNL-CAM5.1, GFDL-AM3, and GEOS-5.

In all analyses, the climatology period was set to the entire analyzed period in each dataset and all anomalies were obtained from the deviations from their climatological means. We defined winter as the three months from December to February for atmospheric variables. It should be noted that seasonal means were calculated from the monthly data during winter and seasonal anomalies were obtained by subtracting seasonal means from the total winter-mean field. The linear trend was calculated based on the linear regression analysis and all statistical significance tests were based on the Student's t test.

The Arctic oscillation index

The Arctic oscillation (AO) index was defined as the leading principal component time series from the empirical orthogonal function (EOF) analysis using the sea level pressure (SLP) anomalies north of 20°N in the boreal winter (DJF)[1]. The overall results are consistent if the AO index is derived from the EOF analysis using the 1000hPa geopotential height. All DJF AO indices (1958–2017) derived from NCEP/NCAR reanalysis 1, JRA-55 reanalysis, and HadSLP2 are highly correlated with the DJF AO index provided by the National Oceanic and Atmospheric Administration (NOAA) Climate Prediction Center with correlation coefficients of 0.96, 0.98, and 0.95, respectively. The linear trend of the AO index is calculated based on the linear regression analysis.

Pacemaker experiments using GRIMs

We conducted the sensitivity experiments using an AGCM, i.e., Global/Regional Integrated Model system (GRIMs)[41,72]. The GRIMs was developed for global and regional scale weather forecasts, climate research, and seasonal simulations[41]. The GRIMs has been widely used throughout many previous studies on the global and regional climate[73–76], and it has been shown in the recent literature[72] that the GRIMs with a chemistry interaction can satisfactorily simulate past (1960–2010) climatological atmospheric features and atmospheric teleconnections due to tropical SST forcing under the Chemistry Climate Model Initiative reference forcing (CCMI REF-C1)[77]. In this study, the horizontal resolution is about 200 km (T62), and 28 vertical layers (L28) with a model top at 3 hPa is used. The physics packages used in this study are the standard versions, which consist of the simplified Arakawa-Schubert convection scheme, Weather Research Forecast (WRF) single-moment microphysics 1, gravity wave drag by orography and convection, short and long wave radiation schemes, and YSU planetary boundary layer scheme. The details of these schemes are described in ref. [41].

We used the monthly Met Office Hadley Centre's SST (HadISST) and SIC data set[35] to prescribe the historical and climatological SST and SIC. The overall experimental structure is similar to that of ref. [78]. The integration

period in all experiments was set to 1948–2018 with 10 ensemble members. We analyzed the last 60-years (1958–2017), which was the same period in the analyses of the reanalysis datasets. To remove the effects of changes in the SIC and CO_2 concentration, we prescribed the monthly climatological SIC with a seasonal cycle and fixed the CO_2 concentration (348 ppm) in all experiments. We conducted six experiments using GRIMs AGCM. (Supplementary Table 2). In the control experiment (CTRL_run), the historical SST is prescribed in the globe. The IO experiment (IO_run) is the same as in the CTRL_run, except the historical SST is prescribed in the tropical Indian Ocean only. The climatological SST with seasonal cycle is prescribed outside the tropical Indian Ocean region. In the same manner, the historical SST is prescribed in the tropical western Pacific in the WP_run, the tropical eastern Pacific in the EP_run, and the tropical Atlantic Ocean in the AT_run. For continuity between historical and climatological SST regions in pacemaker experiments, a linear interpolation is applied within 5° of the boundaries between the historical and climatological SST regions. We displayed the details of geographical regions in which the historical SST is prescribed in each experiment in Supplementary Fig. 5. We also conducted a CLIM_run in which the climatological SST is prescribed in the globe to define a climatology of each atmospheric variable. The climatology of each atmospheric variable is defined as the long-term (60 years) mean of the corresponding atmospheric variables in CLIM_run. All anomalies in the GRIMs experiments are defined as deviations from the climatology of the corresponding atmospheric variables. Supplementary Table 2 summarizes all experiments including CTRL, IO, WP, EP, AT, and CLIM.

Budget diagnostics of zonal mean zonal wind

Budget diagnostics of zonal mean zonal wind is applied to investigate which process is responsible for the change in zonal-mean zonal wind. The equation for the zonal-mean zonal wind can be written as follows[49]:

$$\frac{\partial \langle \overline{u} \rangle}{\partial t} = -\left(\frac{\langle \overline{v} \rangle}{a} \frac{\partial \langle \overline{u} \rangle}{\partial \Phi} + \langle \overline{\omega} \rangle \frac{\partial \langle \overline{u} \rangle}{\partial p} \right) + \left(f + \frac{\langle \overline{u} \rangle \sin \Phi}{a \cos \Phi} \right) \langle \overline{v} \rangle$$
$$- \frac{1}{a \cos^2 \Phi} \frac{\partial}{\partial \Phi} (\langle \overline{u}^* \overline{v}^* \rangle \cos^2 \Phi) - \frac{\partial}{\partial p} \langle \overline{u}^* \overline{\omega}^* \rangle \qquad (1)$$
$$- \frac{1}{a \cos^2 \Phi} \frac{\partial}{\partial \Phi} (\langle \overline{u'v'} \rangle \cos^2 \Phi) - \frac{\partial}{\partial p} \langle \overline{u'\omega'} \rangle - \langle \overline{Du} \rangle$$

where brackets denote a zonal mean, asterisks denote deviations from the zonal mean, overbars denote a monthly mean, and primes denote deviations from the monthly mean. The variables u, v, and ω are zonal wind, meridional wind, and vertical pressure velocity, respectively; a is the radius of the earth, Φ is latitude, p is pressure, f is the Coriolis parameter, and $\overline{D \langle u \rangle}$ is a damping. The first and second terms on the right side of the equation are the advection of the zonal-mean wind by the mean meridional circulation (MMC_{ADV}) and the Coriolis torque (CT), respectively. The third and fourth terms are the forcing by convergence of momentum flux by the stationary waves (CMF_{SW}), and each third and fourth terms are associated with the horizontal (CMF_{SWhor}) and vertical components (CMF_{SWver}) of CMF_{SW}, respectively. The fifth and sixth terms are the forcing by convergence of momentum flux by the transient eddies (CMF_{TR}), and each fifth and sixth terms are also associated with the horizontal (CMF_{TRhor}) and vertical (CMF_{TRver}) components of CMF_{TR}, respectively.

The vertical wave activity flux

The vertical wave activity flux (WAF_z) is calculated to investigate the vertical propagation of planetary waves. The vertical component of wave activity flux is defined as follows[79]:

$$WAF_z = p \cos \Phi \frac{2\Omega^2 \sin^2 \Phi}{N^2 a \cos \Phi} \left(\frac{\partial \psi^*}{\partial \lambda} \frac{\partial \psi^*}{\partial z} - \psi^* \frac{\partial^2 \psi^*}{\partial \lambda \partial z} \right) \qquad (2)$$

where asterisks denote deviations from the zonal mean, ψ is streamfunction, N^2 is the Brunt Väisälä frequency, a is the radius of the earth, Ω is rotation rate of the Earth, λ is longitude, z is vertical level, and p is pressure.

DATA AVAILABILITY

The HadSLP2 dataset is available online (https://www.metoffice.gov.uk/hadobs/hadslp2/). The NCEP/NCAR R1 and JRA-55 reanalysis datasets are available online (https://psl.noaa.gov/data/gridded/data.ncep.reanalysis.html and https://rda.ucar.edu/datasets/ds628.0/, respectively). The HadISST and ERSSTv5 datasets are available online (https://www.metoffice.gov.uk/hadobs/hadisst/ and https://psl.noaa.gov/data/gridded/data.noaa.ersst.v5.html, respectively). Each AMIP-type simulation from NOAA

FACTS is available online (https://psl.noaa.gov/repository/facts). Any request for the GRIMs simulations for the pacemaker experiments should be addressed to jyc0122@hanyang.ac.kr.

CODE AVAILABILITY

All the python codes used to generate the results of this study are available from the authors upon request.

REFERENCES

1. Thompson, D. W. & Wallace, J. M. The Arctic Oscillation signature in the wintertime geopotential height and temperature fields. *Geophys. Res. Lett.* **25**, 1297–1300 (1998).
2. Thompson, D. W. & Wallace, J. M. Annular modes in the extratropical circulation. Part I: Month-to-month variability. *J. Clim.* **13**, 1000–1016 (2000).
3. Thompson, D. W. & Wallace, J. M. Regional climate impacts of the Northern Hemisphere annular mode. *Science* **293**, 85–89 (2001).
4. He, S., Gao, Y., Li, F., Wang, H. & He, Y. Impact of arctic oscillation on the East Asian climate: a review. *Earth. Sci. Rev.* **164**, 48–62 (2017).
5. Kim, J.-S., Kug, J.-S., Jeong, S.-J., Park, H. & Schaepman-Strub, G. Extensive fires in southeastern Siberian permafrost linked to preceding Arctic Oscillation. *Sci. Adv.* **6**, eaax3308 (2020).
6. Kryjov, V. & Gorelits, O. Wintertime Arctic Oscillation and formation of river spring floods in the barents sea Basin. *Russ. Meteorol. Hydrol.* **44**, 187–195 (2019).
7. Song, L. & Wu, R. Comparison of intraseasonal East Asian winter cold temperature anomalies in positive and negative phases of the Arctic Oscillation. *J. Geophys. Res. Atmos.* **123**, 8518–8537 (2018).
8. Wu, B. & Wang, J. Winter Arctic oscillation, Siberian high and East Asian winter monsoon. *Geophys. Res. Lett.* **29**, 3-1–3-4 (2002).
9. Cohen, J., Foster, J., Barlow, M., Saito, K., & Jones, J. Winter 2009-2010: a case study of an extreme Arctic Oscillation event. *Geophys. Res. Lett.* **37**, L17707 (2010).
10. Feldstein, S. B. The recent trend and variance increase of the annular mode. *J. Clim.* **15**, 88–94 (2002).
11. Fyfe, J., Boer, G. & Flato, G. The Arctic and Antarctic Oscillations and their projected changes under global warming. *Geophys. Res. Lett.* **26**, 1601–1604 (1999).
12. Haszpra, T., Topál, D. & Herein, M. On the time evolution of the Arctic Oscillation and related wintertime phenomena under different forcing scenarios in an ensemble approach. *J. Clim.* **33**, 3107–3124 (2020).
13. Shindell, D. T., Miller, R. L., Schmidt, G. A. & Pandolfo, L. Simulation of recent northern winter climate trends by greenhouse-gas forcing. *Nature* **399**, 452–455 (1999).
14. Miller, R., Schmidt, G. & Shindell, D. Forced annular variations in the 20th century intergovernmental panel on climate change fourth assessment report models. *J. Geophys. Res. Atmos.* **111**, D18101 (2006).
15. Shindell, D. T., Schmidt, G. A., Miller, R. L. & Rind, D. Northern Hemisphere winter climate response to greenhouse gas, ozone, solar, and volcanic forcing. *J. Geophys. Res. Atmos.* **106**, 7193–7210 (2001).
16. Cohen, J., Barlow, M. & Saito, K. Decadal fluctuations in planetary wave forcing modulate global warming in late boreal winter. *J. Clim.* **22**, 4418–4426 (2009).
17. Overland, J. & Wang, M. The Arctic climate paradox: The recent decrease of the Arctic Oscillation. *Geophys. Res. Lett.* **32**, L06701 (2005).
18. Smith, D. M. et al. Robust but weak winter atmospheric circulation response to future Arctic sea ice loss. *Nat. Commun.* **13**, 1–15 (2022).
19. Yang, X.-Y., Yuan, X. & Ting, M. Dynamical link between the Barents–Kara sea ice and the Arctic Oscillation. *J. Clim.* **29**, 5103–5122 (2016).
20. Honda, M., Inoue, J. & Yamane, S. Influence of low Arctic sea-ice minima on anomalously cold Eurasian winters. *Geophys. Res. Lett.* **36**, L08707 (2009).
21. Kim, B.-M. et al. Weakening of the stratospheric polar vortex by Arctic sea-ice loss. *Nat. Commun.* **5**, 1–8 (2014).
22. Seierstad, I. A. & Bader, J. Impact of a projected future Arctic sea ice reduction on extratropical storminess and the NAO. *Clim. Dyn.* **33**, 937 (2009).
23. Wu, Q. & Zhang, X. Observed forcing-feedback processes between Northern Hemisphere atmospheric circulation and Arctic sea ice coverage. *J. Geophys. Res. Atmos.* **115**, D14119 (2010).
24. Allen, R. J. & Zender, C. S. Forcing of the Arctic Oscillation by Eurasian snow cover. *J. Clim.* **24**, 6528–6539 (2011).
25. Cohen, J. L., Furtado, J. C., Barlow, M. A., Alexeev, V. A. & Cherry, J. E. Arctic warming, increasing snow cover and widespread boreal winter cooling. *Environ. Res. Lett.* **7**, 014007 (2012).

26. Henderson, G. R., Peings, Y., Furtado, J. C. & Kushner, P. J. Snow–atmosphere coupling in the Northern Hemisphere. *Nat. Clim. Change* **8**, 954–963 (2018).

27. Cohen, J. & Barlow, M. The NAO, the AO, and global warming: How closely related? *J. Clim.* **18**, 4498–4513 (2005).

28. Cohen, J. et al. Recent Arctic amplification and extreme mid-latitude weather. *Nat. Geosci.* **7**, 627–637 (2014).

29. Thompson, D. W., Wallace, J. M. & Hegerl, G. C. Annular modes in the extratropical circulation. Part II: Trends. *J. Clim.* **13**, 1018–1036 (2000).

30. Allan, R. & Ansell, T. A new globally complete monthly historical gridded mean sea level pressure dataset (HadSLP2): 1850–2004. *J. Clim.* **19**, 5816–5842 (2006).

31. Kalnay, E. et al. The NCEP/NCAR 40-year reanalysis project. *Bull. Am. Meteorol. Soc.* **77**, 437–472 (1996).

32. Kobayashi, S. et al. The JRA-55 reanalysis: General specifications and basic characteristics. *J. Meteorol. Soc. Jpn. Ser. II* **93**, 5–48 (2015).

33. Lin, H., Derome, J., Greatbatch, R. J., Andrew Peterson, K. & Lu, J. Tropical links of the Arctic Oscillation. *Geophys. Res. Lett.* **29**, 4-1–4-4 (2002).

34. Zhang, K., Randel, W. J. & Fu, R. Relationships between outgoing longwave radiation and diabatic heating in reanalyses. *Clim. Dyn.* **49**, 2911–2929 (2017).

35. Rayner, N. et al. Global analyses of sea surface temperature, sea ice, and night marine air temperature since the late nineteenth century. *J. Geophys. Res. Atmos.* **108**, 4407 (2003).

36. Huang, B. et al. Extended reconstructed sea surface temperature, version 5 (ERSSTv5): upgrades, validations, and intercomparisons. *J. Clim.* **30**, 8179–8205 (2017).

37. Dhame, S., Taschetto, A. S., Santoso, A. & Meissner, K. J. Indian Ocean warming modulates global atmospheric circulation trends. *Clim. Dyn.* **55**, 2053–2073 (2020).

38. Hu, S. & Fedorov, A. V. Indian Ocean warming can strengthen the Atlantic meridional overturning circulation. *Nat. Clim. Change* **9**, 747–751 (2019).

39. Roxy, M. K., Ritika, K., Terray, P. & Masson, S. The curious case of Indian Ocean warming. *J. Clim.* **27**, 8501–8509 (2014).

40. Murray, D. et al. Facility for Weather and Climate Assessments (FACTS): A Community Resource for Assessing Weather and Climate Variability. *Bull. Am. Meteorol. Soc.* **101**, E1214–E1224 (2020).

41. Hong, S.-Y. et al. The global/regional integrated model system (GRIMs). *Asia. Pac. J. Atmos. Sci.* **49**, 219–243 (2013).

42. Bader, J. & Latif, M. The impact of decadal-scale Indian Ocean sea surface temperature anomalies on Sahelian rainfall and the North Atlantic Oscillation. *Geophys. Res. Lett.* **30**, 2169–2172 (2003).

43. Hoerling, M. P., Hurrell, J. W. & Xu, T. Tropical origins for recent North Atlantic climate change. *Science* **292**, 90–92 (2001).

44. Hoerling, M. P., Hurrell, J. W., Xu, T., Bates, G. T. & Phillips, A. Twentieth century North Atlantic climate change. Part II: Understanding the effect of Indian Ocean warming. *Clim. Dyn.* **23**, 391–405 (2004).

45. Baldwin, M. P. & Dunkerton, T. J. Propagation of the Arctic Oscillation from the stratosphere to the troposphere. *J. Geophys. Res. Atmos.* **104**, 30937–30946 (1999).

46. Wang, L. & Chen, W. Downward Arctic Oscillation signal associated with moderate weak stratospheric polar vortex and the cold December 2009. *Geophys. Res. Lett.* **37**, L09707 (2010).

47. Li, S., Perlwitz, J., Hoerling, M. P. & Chen, X. Opposite annular responses of the Northern and Southern Hemispheres to Indian Ocean warming. *J. Clim.* **23**, 3720–3738 (2010).

48. Li, S. A comparison of polar vortex response to Pacific and Indian Ocean warming. *Adv. Atmos. Sci.* **27**, 469–482 (2010).

49. Seager, R., Harnik, N., Kushnir, Y., Robinson, W. & Miller, J. Mechanisms of hemispherically symmetric climate variability. *J. Clim.* **16**, 2960–2978 (2003).

50. Garfinkel, C. I., Hartmann, D. L. & Sassi, F. Tropospheric precursors of anomalous Northern Hemisphere stratospheric polar vortices. *J. Clim.* **23**, 3282–3299 (2010).

51. Juzbašić, A., Kryjov, V. & Ahn, J. On the anomalous development of the extremely intense positive Arctic Oscillation of the 2019–2020 winter. *Environ. Res. Lett.* **16**, 055008 (2021).

52. Kretschmer, M., Cohen, J., Matthias, V., Runge, J. & Coumou, D. The different stratospheric influence on cold-extremes in Eurasia and North America. *npj Clim. Atmos. Sci.* **1**, 1–10 (2018).

53. Li, S., Hoerling, M. P., Peng, S. & Weickmann, K. M. The annular response to tropical Pacific SST forcing. *J. Clim.* **19**, 1802–1819 (2006).

54. Jeong, J. I. & Park, R. J. Winter monsoon variability and its impact on aerosol concentrations in East Asia. *Environ. Pollut.* **221**, 285–292 (2017).

55. Lu, S. et al. Impact of Arctic Oscillation anomalies on winter PM2. 5 in China via a numerical simulation. *Sci. Total Environ.* **779**, 146390 (2021).

56. Lu, S., He, J., Gong, S. & Zhang, L. Influence of Arctic Oscillation abnormalities on spatio-temporal haze distributions in China. *Atmos. Environ.* **223**, 117282 (2020).

57. Xiao, D. et al. Plausible influence of Atlantic Ocean SST anomalies on winter haze in China. *Theor. Appl. Climatol.* **122**, 249–257 (2015).

58. Alory, G., Wijffels, S. & Meyers, G. Observed temperature trends in the Indian Ocean over 1960-1999 and associated mechanisms. *Geophys. Res. Lett.* **34**, L02606 (2007).

59. Du, Y. & Xie, S. P. Role of atmospheric adjustments in the tropical Indian Ocean warming during the 20th century in climate models. *Geophys. Res. Lett.* **35**, L08712 (2008).

60. Knutson, T. R. et al. Assessment of twentieth-century regional surface temperature trends using the GFDL CM2 coupled models. *J. Clim.* **19**, 1624–1651 (2006).

61. Rao, S. A. et al. Why is Indian Ocean warming consistently? *Clim. Change* **110**, 709–719 (2012).

62. Schott, F. A., Xie, S. P. & McCreary, J. P. Indian Ocean circulation and climate variability. *Rev. Geophys.* **47**, RG1002 (2009).

63. Zhang, L., Han, W. & Sienz, F. Unraveling causes for the changing behavior of the tropical Indian Ocean in the past few decades. *J. Clim.* **31**, 2377–2388 (2018).

64. Endris, H. S. et al. Future changes in rainfall associated with ENSO, IOD and changes in the mean state over Eastern Africa. *Clim. Dyn.* **52**, 2029–2053 (2019).

65. Sung, H. M. et al. Future changes in the global and regional sea level rise and sea surface temperature based on CMIP6 Models. *Atmosphere* **12**, 90 (2021).

66. Tittensor, D. P. et al. Next-generation ensemble projections reveal higher climate risks for marine ecosystems. *Nat. Clim. Change* **11**, 973–981 (2021).

67. Hurrell, J. W., Hack, J. J., Shea, D., Caron, J. M. & Rosinski, J. A new sea surface temperature and sea ice boundary dataset for the Community Atmosphere Model. *J. Clim.* **21**, 5145–5153 (2008).

68. Meinshausen, M. et al. The RCP greenhouse gas concentrations and their extensions from 1765 to 2300. *Clim. Change* **109**, 213 (2011).

69. Molod, A. et al. *The GEOS-5 Atmospheric General Circulation Model: Mean Climate And Development from MERRA to Fortuna* NASA Technical Report Series on Global Modeling and Data Assimilation NASA/TM-2012-104606-VOL-28, GSFC.TM.01153.2012 (NASA, 2012).

70. Donner, L. J. et al. The dynamical core, physical parameterizations, and basic simulation characteristics of the atmospheric component AM3 of the GFDL global coupled model CM3. *J. Clim.* **24**, 3484–3519 (2011).

71. Neale, R. B. et al. Description of the NCAR community atmosphere model (CAM 5.0). *NCAR Tech. Note NCAR/TN-486+ STR* **1**, 1–12 (2010).

72. Jeong, Y. C., Yeh, S. W., Lee, S. & Park, R. J. A Global/Regional Integrated Model System-Chemistry Climate Model: 1. Simulation Characteristics. *Earth. Space Sci.* **6**, 2016–2030 (2019).

73. Ham, S. & Hong, S.-Y. Sensitivity of simulated intraseasonal oscillation to four convective parameterization schemes in a coupled climate model. *Asia. Pac. J. Atmos. Sci.* **49**, 483–496 (2013).

74. Song, K., Son, S.-W. & Charlton-Perez, A. Deterministic prediction of stratospheric sudden warming events in the Global/Regional Integrated Model system (GRIMs). *Clim. Dyn.* **55**, 1209–1223 (2020).

75. Jang, H.-Y., Yeh, S.-W., Chang, E.-C. & Kim, B.-M. Evidence of the observed change in the atmosphere–ocean interactions over the South China Sea during summer in a regional climate model. *Meteorol. Atmos. Phys.* **128**, 639–648 (2016).

76. Jeong, Y. C., Yeh, S. W., Lee, S., Park, R. J. & Son, S. W. Impact of the stratospheric ozone on the Northern Hemisphere surface climate during boreal winter. *J. Geophys. Res. Atmos.* **126**, e2021JD034958 (2021).

77. Eyring, V. et al. Overview of IGAC/SPARC Chemistry-Climate Model Initiative (CCMI) community simulations in support of upcoming ozone and climate assessments. *SPARC Newsl.* **40**, 48–66 (2013).

78. Chang, E. C., Yeh, S. W., Hong, S. Y. & Wu, R. Sensitivity of summer precipitation to tropical sea surface temperatures over East Asia in the GRIMs GMP. *Geophys. Res. Lett.* **40**, 1824–1831 (2013).

79. Plumb, R. A. On the three-dimensional propagation of stationary waves. *J. Atmos. Sci.* **42**, 217–229 (1985).

ACKNOWLEDGEMENTS

AUTHOR CONTRIBUTIONS

Y.C.J. and S.W.Y. conceived of the study and Y.C.J. conducted analysis and model experiment, and wrote the first manuscript. S.W.Y. edited the manuscript with comments and input from all authors. Y.K.L., A.S. and G.W. edited the manuscript with comments.

COMPETING INTERESTS

The authors declare no competing interests.

ADDITIONAL INFORMATION

Supplementary information The online version contains supplementary material available at https://doi.org/10.1038/s41612-022-00279-x.

Correspondence and requests for materials should be addressed to Sang-Wook Yeh.

Reprints and permission information is available at http://www.nature.com/reprints

Publisher's note Springer Nature remains neutral with regard to jurisdictional claims in published maps and institutional affiliations.